# ADVANCED MATERIALS

## LIVING COMPOSITES

In article number 2006946, Qiming Wang and co-workers present a paradigm to guide living bacteria to grow bionic mineralized composites. The strategy demonstrates a class of living composites with ordered microstructures and exceptional mechanical properties. This research progress highlights an exciting opportunity for future bionic composite materials by tailoring the interaction or communication between living organisms and 3D-printed synthetic materials.
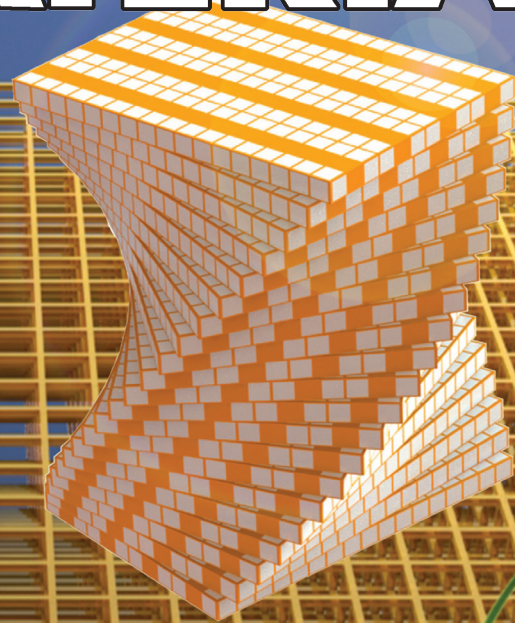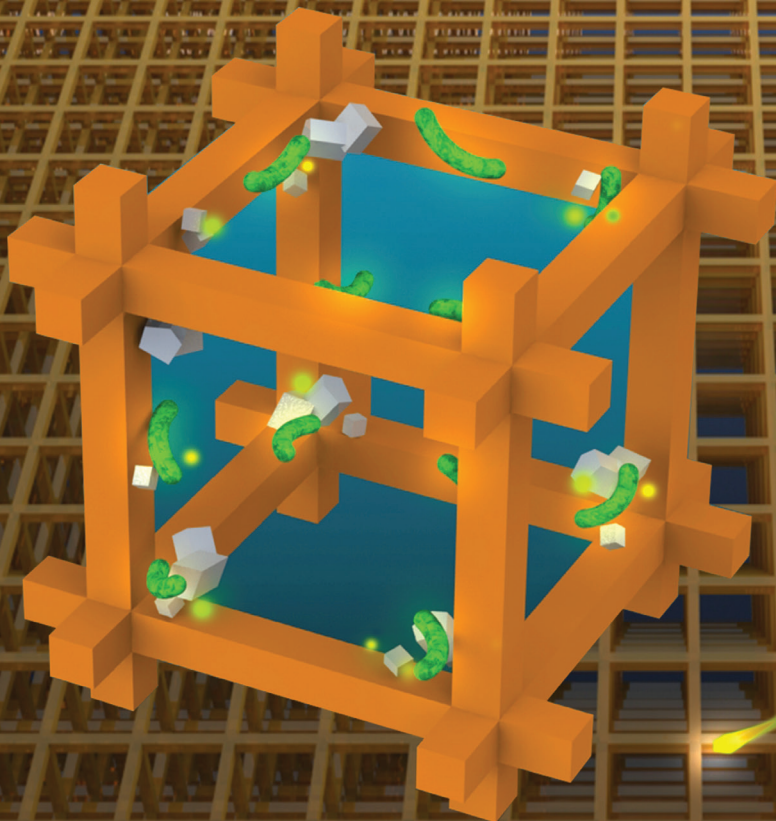
Check for updates

# Growing Living Composites with Ordered Microstructures and Exceptional Mechanical Properties

*An Xin, Yipin Su, Shengwei Feng, Minliang Yan, Kunhao Yu, Zhangzhengrong Feng, Kyung Hoon Lee, Lizhi Sun, and Qiming Wang\**

**Living creatures are continuous sources of inspiration for designing synthetic materials. However, living creatures are typically different from synthetic materials because the former consist of living cells to support their growth and regeneration. Although natural systems can grow materials with sophisticated microstructures, how to harness living cells to grow materials with predesigned microstructures in engineering systems remains largely elusive. Here, an attempt to exploit living bacteria and 3D-printed materials to grow bionic mineralized composites with ordered microstructures is reported. The bionic composites exhibit outstanding specific strength and fracture toughness, which are comparable to natural composites, and exceptional energy absorption capability superior to both natural and artificial counterparts. This report opens the door for 3D-architectured hybrid synthetic–living materials with living ordered microstructures and exceptional properties.**

Designing high-performance structural materials with excellent mechanical properties (such as strength, fracture toughness, and energy dissipation) is a long-standing engineering endeavor. Nature has developed a strategy by intelligently integrating stiff minerals and soft organics in a highly sophisticated manner to produce natural structural composites with ultrahigh strength and fracture resistance.[1–3] The outstanding mechanical properties of these natural structural composites, such as nacres,[4] arapaima scales,[5] and stomatopod dactyl clubs,[6] are primarily due to two key factors: First, the fractions of stiff minerals within these composites are relatively high, for instance, as high as 87.5% by volume (95% by weight) in nacres.[4] Second, the minerals are typically assembled into ordered microstructures to efficiently retard the crack propagation; for example, the minerals within the stomatopod dactyl club display a Bouligand structure with a helicoidal ply orientation.[6] On the side of bionic engineering, though promising structural composites have been fabricated to imitate

their natural counterparts;[1–3] the bionic designs have been bottlenecked due to the competition of two key factors: the fraction of minerals and freedom in controlling mineral orientations (**Figure 1**A and Table S1, Supporting Information). Technologies such as layer-by-layer assembly,[7,8] self-assembly,[9,10] freeze-casting,[11–13] and chemical mineralization[14,15] have produced remarkable structural composites with high mineral volume fractions, but achieving complex mineral orientations (such as helicoidal ply orientations) is challenging (Figure 1A). Recently, field-induced mineral alignment has been integrated with casting to achieve impressive structural composites with complex orders;[16–19] however, casting is not energy-efficient in achieving helicoidal ply orientations (Figure 1A). To overcome the drawback of casting, researchers have employed 3D-printing technologies with the field-assisted alignment to enable high freedom in controlling mineral ply orientations;[20–23] however, the fractions of minerals in the 3D-printing inks are not high (typically <20 vol%, Table S1, Supporting Information), due to the requirement of efficient photopolymerization[20,21,23] or flow[22] during the 3D-printing process (Figure 1A). Therefore, a manufacturing method to allow for both high fractions of minerals and high freedom in controlling mineral orientations remains an outstanding challenge in the field.

Nature has already provided wisdom to address this challenge by directly growing high-fraction minerals in precisely controlled orientations (Figure 1B). When mollusks or arthropods build mineralized composites, an insoluble $\beta$-chitin matrix filled with silk fibroin gel is generated to serve as a scaffold.[24–26] The mineral cores form on the surface of the $\beta$-chitin matrix, starting from the asp-rich glycoproteins that serve as the nucleation sites.[24–26] Then, the mineral will grow along a scaffold-guided pathway to form microstructures with ordered orientations (such as the Bouligand structure in the stomatopod dactyl club,[6] Figure 1B). Despite the high sophistication of the natural growing strategy, translating the strategy to engineering practice is challenging because of the difficulty in guiding the complex natural growing process to precisely follow predesigned pathways.

Inspired by the natural growing strategy, we here propose to harness guided biomineralization within 3D-printed polymer structures to directly grow bionic composites with

A. Xin, Dr. Y. Su, M. Yan, K. Yu, Z. Feng, K. H. Lee, Prof. Q. Wang
Sonny Astani Department of Civil and Environmental Engineering
University of Southern California
Los Angeles, CA 90089, USA
E-mail: qimingw@usc.edu
S. Feng, Prof. L. Sun
Department of Civil and Environmental Engineering
University of California, Irvine
Irvine, CA 92697, USA

The ORCID identification number(s) for the author(s) of this article can be found under https://doi.org/10.1002/adma.202006946.

**ADVANCED
SCIENCE NEWS**

www.advancedsciencenews.com
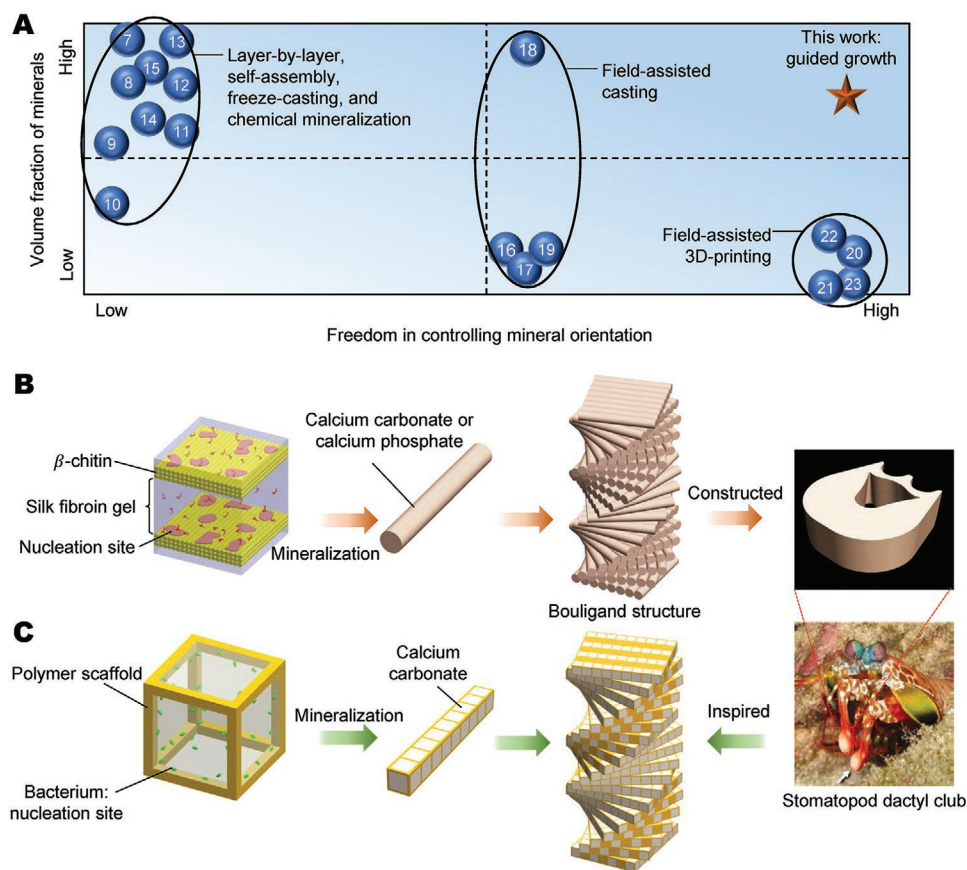
**ADVANCED
MATERIALS**

www.advmat.de

**Figure 1.** Conceptual idea. A) A diagram to show the relationship between the volume fraction of minerals and the freedom in controlling mineral orientation within structural composites. The numbers in blue circles are reference numbers. More information is shown in Table S1, Supporting Information. B) Schematics to show the production process of mineralized structural composites in living creatures (such as stomatopod dactyl club). C) Schematics to show the proposed strategy for growing bionic composites in this work: bacteria-assisted mineral growth within a 3D-printed scaffold. Image of the stomatopod dactyl club: Reproduced with permission.[6] Copyright 2012, American Association for the Advancement of Science.

high fractions of minerals (45–90 vol%) and nearly arbitrary mineral orientations (Figure 1C; Movie S1, Supporting Information). The method relies on a 3D-printed polymer scaffold to mimic the structured $\beta$-chitin matrix, and bacteria attached on the polymer surface to serve as nucleation sites. The enzyme urease secreted by the bacteria assists the mineralization of calcium carbonate ($CaCO_3$) that grows around the polymer scaffold. The mineral growth is guided by micropores within the scaffold, eventually leading to bionic mineralized composites with predesigned microstructures. The growing process is understood with an analytical theory and a phase-field model. The bionic mineralized composites exhibit outstanding specific strength and fracture toughness that are comparable to natural composites, and exceptional energy absorption capability that is superior to both natural and artificial counterparts.

The manufacturing strategy primarily relies on bacteria-assisted mineral growth within 3D-printed microporous lattice scaffolds. Although the bacteria-assisted mineralization has been previously used to heal cementitious materials,[27,28] harnessing guided bacterial mineralization to design structural composites has not been explored. The overall experimental procedure of the proposed method is shown in Movie S1, Supporting Information. We first 3D-print a cubic polymer

lattice with beam diameter $\approx 100$ μm and unit cell size $\approx 500$ μm (**Figure 2**A,B). Then, we immerse the lattice in a bacterial medium to allow for the attachment of bacteria (*S. pasteurii*) to the internal lattice surface. Subsequently, the lattice is immersed in a mineralization medium with urea and $Ca^{2+}$ to enable the mineral growth within the lattice. The bacteria play two roles during the mineralization process: First, the bacteria secrete urease that can catalyze the decomposition of urea to form $CO_3^{2-}$, which reacts with $Ca^{2+}$ to form $CaCO_3$.[27,28] Second, the bacteria attached to the internal lattice surface serve as nucleation sites to initiate the mineralization of $CaCO_3$ crystals around the lattice surface,[29] followed by gradually filling up the void space. Note that directly using urease to form $CaCO_3$ cannot initiate the mineralization starting from the lattice surface.[29] In the experiment, more and more white $CaCO_3$ minerals fill the free space over days (Figure 2B). The phenomenon is observed by optical microscopy and scanning electron microscopy (SEM) on the lattice beams (Figure 2CD). A small number of mineral nuclei randomly appear on the lattice beam surface on day 2; after 6 days, the lattice beam surface is entirely wrapped with minerals. The $CaCO_3$ minerals are primarily in the form of calcite.[30–33] The volume coverage of the minerals keeps increasing over 10 days until the lattice voids
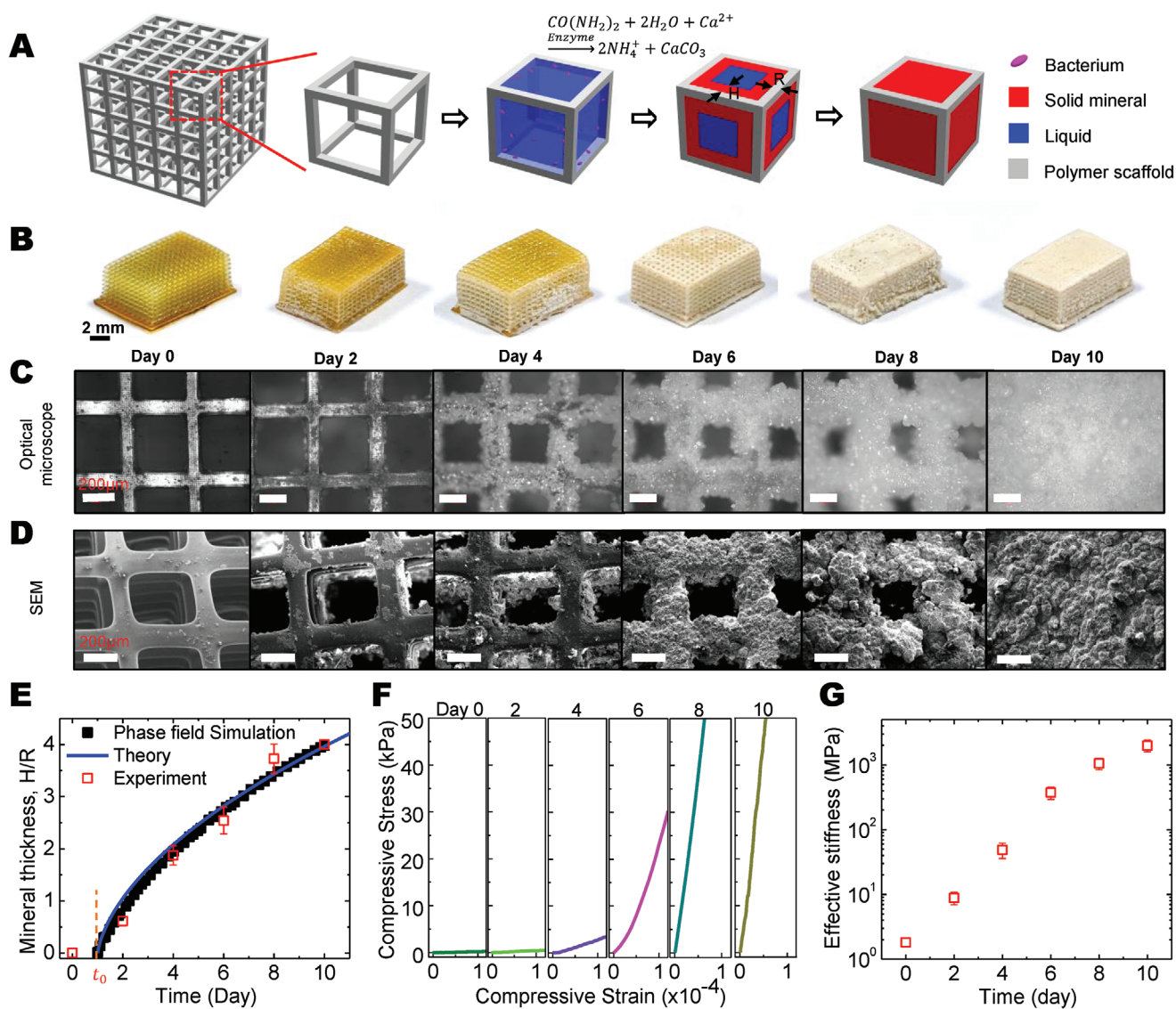
**Figure 2.** Bacteria-assisted mineral growth within a lattice scaffold. A) Schematics to show the bacterial-assisted mineral growth process. $H$ is the mineral thickness and $R$ is the half beam width. B–D) Samples (B), their optical microscopic images (C), and their SEM images (D) during the bacteria-assisted mineral growth process over 10 days. E) Experimentally observed, phase-field simulated, and theoretically calculated normalized mineral thickness in functions of time. F) The relationships between compressive stress and strain of the mineralized sample over 10 days. G) Young's modulus of the mineralized sample over 10 days. The error bars are standard deviations of 3–5 tests.

are fully filled (Figure 2E). To quantify the mechanical behavior of the mineralized samples over experimental days, we employ compressive tests to measure their stiffness (Figure 2F). We find that the effective stiffness of the virgin lattice structure on day 0 is 1.82 ± 0.28 MPa; however, the effective stiffness of the mineralized sample on day 10 increases to 1.99 ± 0.4 GPa, with an increasing factor of three orders of magnitude (Figure 2G).

To understand the bacteria-assisted mineral growth, we first focus on the mineral growth around a polymer beam with a square cross-section (dimension $2R \times 2R$) (**Figure 3**A). After the polymer lattice is immersed in the mineralization medium, bacteria secrete urease to catalyze the formation of solute $CaCO_3$.[27,28] When solute $CaCO_3$ is oversaturated, the bacteria attached to the lattice beam surface initiate the mineralization

of $CaCO_3$ crystals. When the solute $CaCO_3$ is consumed around the lattice beam, more solutes in the solution need to diffuse to the beam surface to support the further mineralization process; therefore, the mineral growth is governed by the solute diffusion.[34,35] To analytically model the mineral growth, we approximate the square cross-section as a circle with a diameter of $2R$ and develop a theory to formulate the mineral thickness $H$, written as $H/R = G(D(t - t_0)/R^2, \alpha)$ (Figure 3A and Figure S1, Supporting Information),[34,35] where $t$ is the time in the mineralization medium, $t_0$ is the initiation time for the mineral growth, $D$ is the diffusivity of solute $CaCO_3$ in the solution, and $\alpha$ is a parameter related to the concentration of the oversaturated $CaCO_3$. Note that the cross-section approximation can be verified by phase field simulations (Figure S2, Supporting
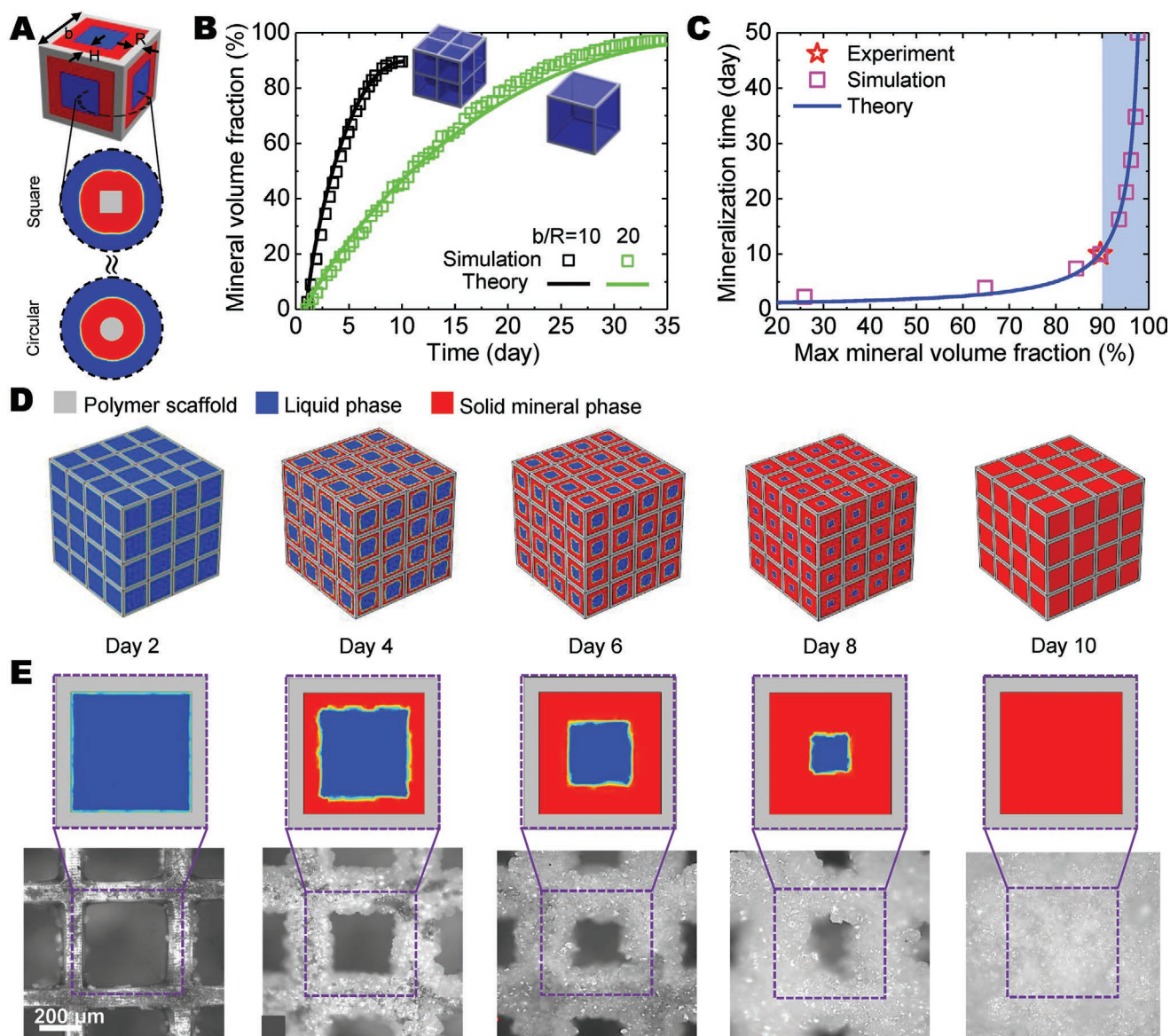
**Figure 3.** Modeling of mineral growth. A) Schematics to illustrate the mineral growth around a lattice beam with a square cross-section. $b$ is the unit size, $H$ is the mineral thickness, and $R$ is the half beam width. It can be approximated as the mineral growth around a circular beam with a radius of $R$. B) Numerically simulated and theoretically calculated mineral volume fractions of two lattices ($b/R = 10$ and 20) in functions of mineralization time. C) The maximal mineral volume fractions after fully filling the lattice scaffolds in a function of the required mineralization time. D) Numerically simulated mineral growth over 10 days using phase-field modeling. E) Comparison between the numerically simulated and experimentally observed mineral–polymer units over 10 days.

Information). By selecting $t_0 = 1$ day, the analytical model can quantitatively explain the experimentally observed mineral thickness over 10 days (Figure 2E). Although the theory is originally planned to explain the mineral growth around a single beam, it also shows a good agreement with experimental results when the lattice void is almost fully filled by the minerals (i.e., day 10, Figure 2E).

For a cubic unit cell with a beam diameter of $2R$, unit size of $b$, and mineral thickness of $H$, the mineral volume fraction is calculated as

$$\eta = \frac{\left[8(1+H/R)^3 + 12(b/R - 2 - 2H/R)(1+H/R)^2\right] - \left[12b/R - 16\right]}{(b/R)^3} \quad (1)$$

With Equation (1), the analytical theory reveals that the mineral volume fraction grows more rapidly with decreasing unit cell size (Figure 3B); this is because a smaller unit cell size within the periodic lattice structure is corresponding to a larger relative internal surface area to facilitate the bacteria-assisted mineral growth (see insets of Figure 3B). When $H/R = b/(2R) - 1$, the lattice void is fully filled by minerals. The maximal mineral volume fraction $\eta_*$ can be calculated as a function of the required mineralization time $t_*$. The theory reveals that $t_*$ first increases slowly with increasing $\eta_*$ and then increases rapidly after $\eta_* = 90\%$ and $t_* = 10$ day (Figure 3C). We indeed select this critical mineral volume fraction ($\eta_* = 90\%$ and $b/R = 10$) to carry out the experiments (Figure 2).
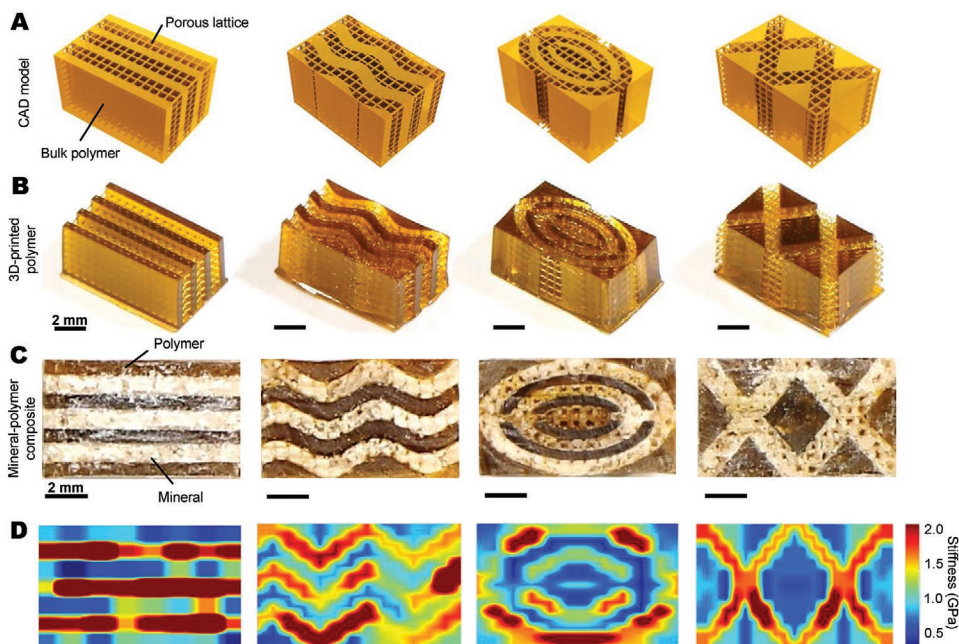
**Figure 4.** Bionic mineralized composites with selective mineralization. A) Computer-aided design (CAD) models for polymer scaffolds. B) 3D-printed polymer scaffolds. C) Bionic mineralized composite samples. D) Stiffness mapping of the bionic mineralized composites. The inhomogeneity of the stiffness distribution may be attributed to inhomogeneous mineralization within the lattice regions.

To further verify the theoretical and experimental results, we develop a phase-field simulation framework to study the mineral growth (Figure 3D).[36,37] This simulation includes two variables: the phase field $\phi(\mathbf{x}, s)$ and the concentration field $c(\mathbf{x}, s)$ of $CaCO_3$, where $\mathbf{x}$ is the position vector and $s$ is the time starting from the mineral growth (i.e., $s = t - t_0$ in Equation (1)). The variable $\phi(\mathbf{x}, s)$ is an ordering parameter, with $\phi = 0$ corresponding to the liquid phase of $CaCO_3$ and $\phi = 1$ the solid phase. The Helmholtz free energy of the system is (Supporting Information):[36]

$$F(\phi,c) = \int_\Omega \left[ f(\phi,c) + \frac{1}{2}\varepsilon^2(\nabla\phi)^2 + \frac{1}{2}k_c(\nabla c)^2 \right] d\Omega \qquad (2)$$

where $\Omega$ is the region occupied by the system, $f(\phi,c)$ is the Helmholtz free energy density for a phase with no gradient, $\varepsilon$ is a small parameter which determines the thickness of the interface of the two phases, and $k_c$ is the interfacial coefficient. The phase-field simulation can nicely reveal the mineral growth within the cubic lattice structure (Figure 3D and Movie S2, Supporting Information). The geometry and thickness of the formed mineral around the lattice beam resemble those in the experiments from day 2 to day 10 (Figures 3E and 2E). In addition, the phase-field simulation can consistently verify the theory for the mineral growth within lattices with various unit sizes (Figure 3B and Figure S3, Supporting Information). The simulated required time for full mineralization also agrees well with the theoretical results (Figure 3C).

The mineral growth within porous lattices can be harnessed to manufacture bionic mineralized composites with complex integration architectures (**Figure 4**). The mechanism relies on the judicious arrangement of two phases, porous polymer lattice and bulk polymer, within a 3D-printed scaffold (Figure 4A,B). We first enable the bacterial attachment on the beam surfaces of the porous lattice region. Then, we cover the polymer scaffold with a permeable fabric and immerse it into the mineralization medium. Because the porous lattice phase provides free space, the minerals grow within the lattice region, but not around the bulk polymer region (Movie S1, Supporting Information). After 10 days, the lattice region is filled with white $CaCO_3$ minerals (Figure 4C). The cross-section SEM images show the clear boundaries between the mineral and polymer phases (Figure S4, Supporting Information). During the mineralization process, the effective stiffness of the porous lattice region drastically increases (Figure 2G), while the stiffness of the bulk polymer region maintains. We employ indentation tests to measure the local stiffness on the sample surfaces (Figure S5, Supporting Information). Indentation tests show that the stiffness of the mineralized region (previously lattice region) reaches as high as 2.3 GPa, around 5 times the stiffness of the bulk polymer region (≈400 MPa) (Figure 4D). Note that the arrangement of two phases is fully determined by the customized design; thus, this method may be able to generate mineralized composites with nearly any locations of selective mineralization, such as straight lines, wavy curves, circles, and crossing lines as shown in Figure 4. The minimal width of the mineralized region is determined by the unit cell size of the lattice (≈500 μm in Figure 4).

The mineral growth within porous lattices can be further harnessed to manufacture bionic mineralized composites with various mineral ply orientations (**Figure 5**). The mechanism is to utilize porous lattice channels to grow mineral fibers. The fiber orientation is denoted as the angle with the x-axis (Figure 5A). The whole composite consists of multiple
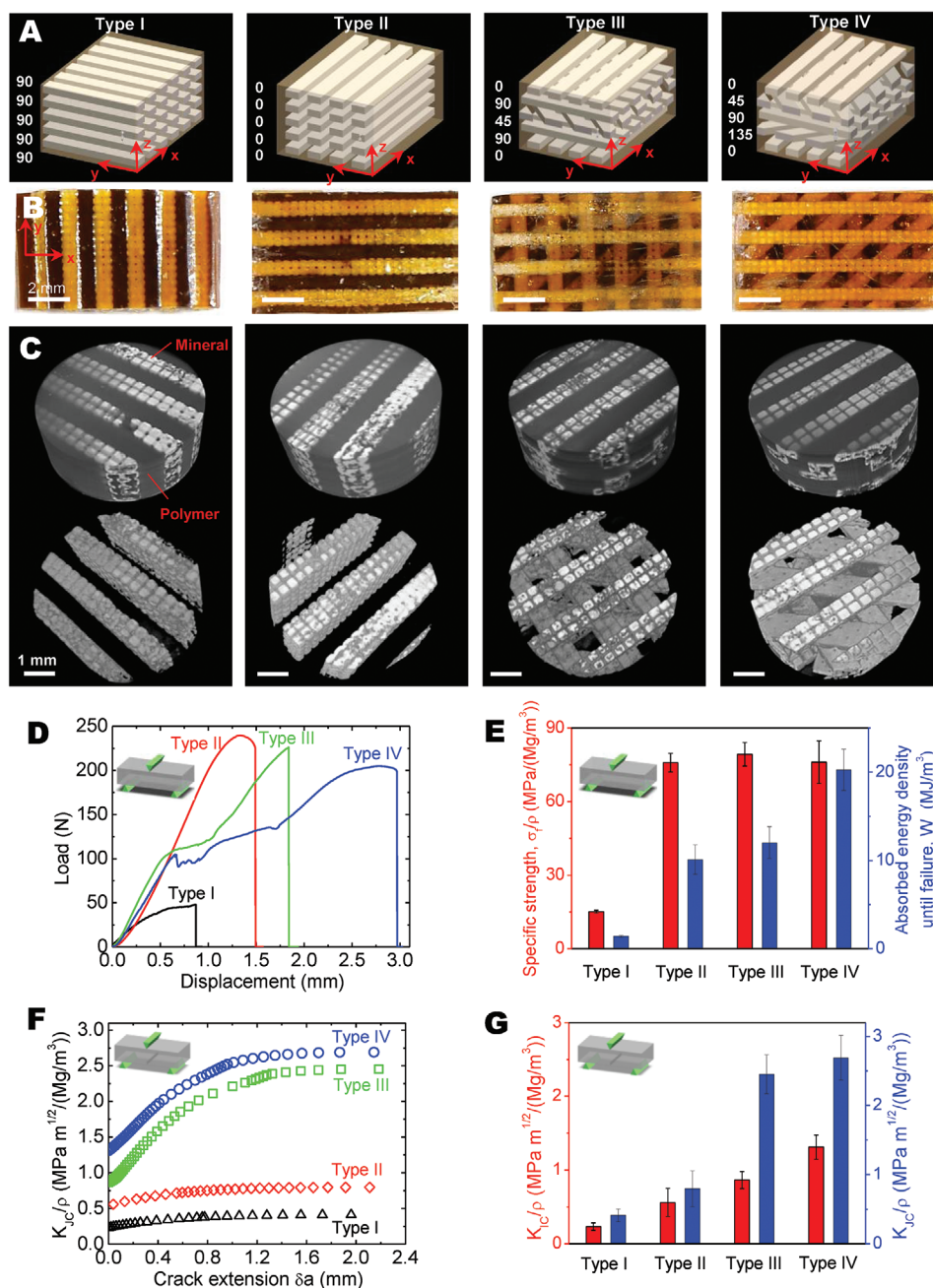
**Figure 5.** Bionic mineralized composites with various mineral ply orientations. A) Schematics to illustrate ply orientations of mineral fibers on different layers of composites. The orientation angle is defined as the angle with the x-axis. Four types of composites show different ply orientations. B) Bionic mineralized composite samples. C) Micro-CT scanned images of bionic composites and the mineral phases. D) Load–displacement curves of mineral-polymer composites under three-point bending tests. The inset shows the schematic for the three-point bending test. E) Specific strengths ($\sigma_f/\rho$) and absorbed energy densities until failure ($W_a$) of four types of bionic composites under three-point bending tests. The absorbed energy until failure is the enclosed area of the load–displacement curves in (D). F) Crack-resistance curves (R-curves) in terms of the specific stress intensity ($K_{JC}/\rho$) as a function of crack extension ($\Delta a$) for four types of bionic composites. The inset shows the schematic for the single-notched bending test. G) Specific fracture toughness for crack initiation ($K_{IC}/\rho$) and stable crack propagation ($K_{JC}/\rho$) of four types of composites. The error bars are standard deviations of 3–5 tests.

layers, where the fiber orientation on a different layer can be different. Here, we focus on four types with fiber orientations as (Figure 5A): [90, 90, 90, 90, 90] (type I), [0, 0, 0, 0, 0] (type II), [0, 90, 45, 90, 0] (type III), and [0, 45, 90, 135, 0] (type IV). In experiments, we first 3D-print polymer structures with porous

lattice channels with different orientations on different layers (Figure S6A–C, Supporting Information), and then allow for the bacteria-assisted selective growth of $CaCO_3$ minerals within the lattice channels over 10 days (Figure 5B). Micro-computed tomography (Micro-CT) scanning is employed to

**ADVANCED
SCIENCE NEWS**

www.advancedsciencenews.com

**ADVANCED
MATERIALS**

www.advmat.de

characterize the internal microstructures of two phases within the composite matrix (Figure 5C and Movies S3–S6, Supporting Information). The CT scanning images clearly display the ply orientations of mineral fibers on different layers. Besides, since the mineral growth is initiated from the surface-attached bacteria, the formed minerals are firmly bonded on the polymer surface,[29] which can be revealed from the CT scanning images (Figure 5C) and interfacial SEM images (Figure S4, Supporting Information).

We first use three-point-bending (3PB) tests to quantify the mechanical strength of the bionic mineralized composites (inset of Figure 5D; sample geometry in Table S2, Supporting Information). The supporting span is along the x-axis, and the load is along the z-axis. The load–displacement curves for different types of composites are shown in Figure 5D. The maximal load is used to compute the specific flexural strength $\sigma_f/\rho$, where $\sigma_f$ is the flexural strength and $\rho$ is the effective density (Figure 5E). The enclosed area of the load–displacement curve is used to calculate the absorbed energy density until failure $W_a$ (Figure 5E). As comparisons, the specific flexural strengths and the absorbed energy densities until failure of the pure mineral, the pure polymer, and the mineral–polymer fiber are shown in Figure S7, Supporting Information. We find that the maximal load of types II, III, and IV composites are much larger than that of type I, because the fracture in type I composite may only propagate within the polymer matrix or along the polymer-mineral interface, while the fractures in other types need to break mineral fibers on multiple layers. Especially, the maximal load of type II is the highest because the fracture needs to break mineral fibers on each layer. In terms of energy absorption capability, type IV is the highest because the mineral fiber orientation displays a Bouligand structure, resembling the helicoidal mineral structures in the stomatopod dactyl club.[6] Once the fracture occurs, twisting cracks can be developed due to the orientation distribution of mineral fibers, and the propagation of these cracks will make a significant contribution to the internal energy dissipation.[38–40] As a result, Bouligand-like type IV structure features a remarkable energy absorption capability (Figure 5E), around 20 times that of type I and 2 times that of type II.

To further quantify the crack resistance of the bionic mineralized composites, we employ single notched bending (SNB) tests to measure the fracture toughness to resist crack initiation and propagation (inset of Figure 5F; Figure S6D, Supporting Information).[10,12,13,41,42] The crack resistance curves (R-curves) of four types show a similar behavior: fracture toughness increases from the initial fracture toughness ($K_{IC}$) as the crack extends and approaches a plateau ($K_{JC}$) when the crack stably propagates (Figure 5F,G). The fracture toughness of type I is the lowest because the fracture propagates within the polymer matrix or along the polymer–mineral interface. The fracture toughness of type II is larger than that of type I, because the fracture in type II needs to break both polymer and mineral phases. Along with the crack extension, the fracture toughnesses of types I and II slightly increase and reach their plateaus after a short crack extension (0.4–0.6 mm); for example, the plateau $K_{IC}/\rho$ of types II is only 40% higher than its $K_{IC}/\rho$. However, the fracture toughnesses of types III and IV reach their plateaus after a long crack extension (1.2–1.4 mm) and the plateaus $K_{IC}/\rho$ are higher than their $K_{IC}/\rho$ by 185% and 107%, respectively. This drastic difference in the crack resistance is attributed to the difference in their mineral ply orientations. In types I and II, the materials at the rear and front of the crack tip are homogeneous, and the crack can thus easily propagate once initiated. However, the heterogeneous mineral ply orientations of types III and IV, resembling the Bouigand structure in stomatopod dactyl club,[6] can efficiently bend, twist, and retard the crack propagation.[38–40]

To compare the presented bionic mineralized composites with natural and artificial structural composites, we construct two Ashby diagrams shown in **Figure 6** (data in Table S3, Supporting Information). Figure 6A shows the relationship between specific flexural strength ($\sigma_f/\rho$) and specific plateau fracture toughness ($K_{JC}/\rho$). The bionic mineralized composites (type IV in Figure 5) feature $\sigma_f/\rho$ of 76 ± 8.7 MPa/(Mg m$^{-3}$) and $K_{JC}/\rho$ of 2.63 ± 0.3 MPa m$^{1/2}$/(Mg m$^{-3}$), which are comparable to the natural composites (such as natural nacres[10,15,23]) and other state-of-the-art artificial structural composites, such as calcium phosphate–alginate composites,[10] alumina–poly(methyl methacrylate) composites,[12] calcium
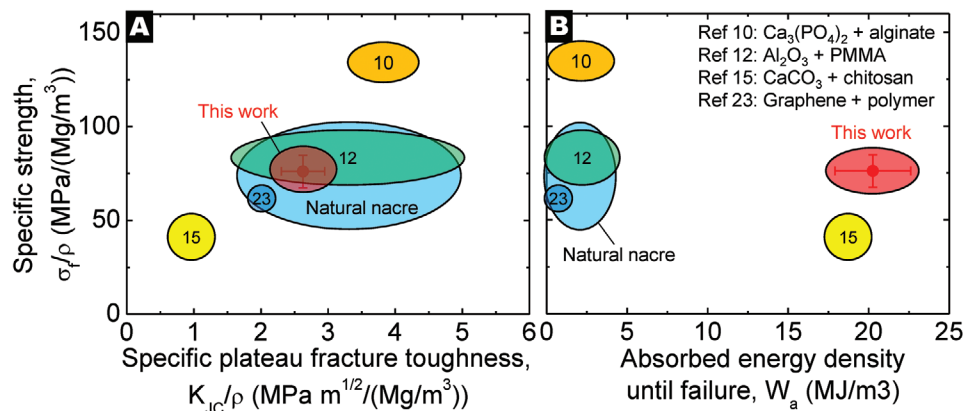


**Figure 6.** Comparison of mechanical properties of the bionic mineralized composites and natural and artificial composites. A) Ashby diagram of specific strength versus specific fracture toughness of the bionic composites (type IV) compared with natural nacre and other artificial mineralized composites. B) Ashby diagram of absorbed energy density until failure of the bionic composites (type IV) compared with their competitors. The numbers in circles are reference numbers.

carbonate–chitosan composites,[15] and graphene–polymer composites.[23] Figure 6B shows the relationship between the specific flexural strength ($\sigma_f/\rho$) and the absorbed energy density until failure ($W_a$). The bionic mineralized composites (type IV in Figure 5) feature $W_a$ of 20.26 ± 2.35 MJ m$^{-3}$, which is almost an order higher than those of natural nacres[10,23] and most of the existing artificial structural composites.[10,12,23] Although the energy absorption capability of the bionic composite in this work is only slightly higher than that of the reported calcium carbonate–chitosan composites (≈19 MJ m$^{-3}$) (Figure 6B),[15] the specific fracture toughness of the bionic composite is 150% higher and the specific flexural strength is 60% higher (Figure 6A).

In summary, we present a strategy to manufacture bionic mineralized composites by harnessing bacteria-assisted mineralization within 3D-printed polymer scaffolds. Compared to other existing methods, our bionic method can produce mineralized composites with high fractions of minerals (45–90 vol%) and highly ordered mineral orientations (Figure 1A). Due to the ordered orientations of minerals, the bionic composites feature an exceptional combination of specific strength, specific fracture toughness, and energy absorption capability (Figure 6). The present material system harnesses the guided bacteria-assisted growth of minerals within polymer structures to produce a living bionic material system, whose growing feature is drastically different from most of the existing fabrication methods. This strategy highlights an exciting opportunity for future hybrid synthetic–living bionic materials[43–47] by tailoring interactions or communications between living organisms and 3D-printed synthetic materials. The manufacturing strategy can be easily extended by selectively controlling the activity of living organisms to synthesize unprecedented structural composites with ordered, hierarchical, and gradient microstructures.

## Experimental Section

*Materials*: Tough resin (a mixture of (meth)acrylated monomers, (meth)acrylated oligomers, and photo initiators) was purchased from Formlabs. It was selected because of two reasons: 1) the tough resin showed an outstanding toughness, and 2) the employed bacteria could be easily attached on the tough resin. Dimethylacetamide (DMA), phenylbis(2,4,6-trimethylbenzoyl)phosphine oxide (photoinitiator), Sudan I (photo absorber), hydrochloric acid, and ethanol were purchased from Sigma-Aldrich. *Sporosarcina pasteurii* (ATCC 11859) was purchased from ATCC. To prepare the BPU medium (ATCC 1832) and the mineralization medium, tryptone, ammonium sulfate, ammonium chloride, sodium bicarbonate, and calcium chloride were purchased from Sigma-Aldrich. Urea, tricine, yeast extract, agar, and L-glutamic acid were purchased from Alfa Aesar. Difco Nutrient Broth was purchased from Fisher Scientific. All chemicals were used without further purification.

*3D-Printing of Polymer Scaffolds*: Tough resin (6 g) was first mixed with DMA solvent (3 g) by magnetically stirring for around 1 h. Thereafter, 0.09 g photoinitiator and 0.01 g Sudan I were added into the solution and stirred for another 1 h. The additive manufacturing was performed with tough resin in a stereolithography system. A computer-aided-design model was sliced into sequential images that were projected to a liquid basin. The exposed resin was solidified by light exposure, forming a solid layer bonded onto the printing stage. As the printing stage was lifted, the fresh resin refluxed beneath the printing stage. By lowering down the stage a prescribed height and illuminating the resin with another slice image, a second layer was printed and bonded onto the first layer. These processes were repeated until the whole structure was printed. Each layer was set as 28 µm thickness and required 14 s to solidify.

Subsequently, the 3D-printed polymer was washed by pure ethanol and dried in air at 70 °C for 24 h to evaporate the DMA solvent.

*Bacteria-Assisted Mineralization*: BPU medium (ATCC 1832 medium) containing 10 g L$^{-1}$ tryptone, 5 g L$^{-1}$ yeast extract, 4.5 g L$^{-1}$ tricine, 5 g L$^{-1}$ ammonium sulfate, 2 g L$^{-1}$ glutamic acid, and 10 g L$^{-1}$ urea was adjusted to pH 8.6 ± 0.1 using a NaOH solution, and then filter-sterilized with a 0.2 µm sterile filter. The mineralization medium was prepared by dissolving 3 g Difco nutrient broth, 20 g urea, 10 g ammonium chloride, and 2.12 g sodium bicarbonate into 1 L deionized water. After adjusting the pH below 6.0, the medium was autoclaved at 121 °C and 21 psi for 45 min. 28 g CaCl$_2$ was dissolved into the cooled, heat sterilized solution. The dried samples were first soaked in 150 mL BPU medium with bacteria for 24 h at 30 °C. Subsequently, the structures were immersed in 150 mL mineralization medium in an incubator at 28 °C, 50 rpm. The medium was refreshed every day. Samples were taken out after 10 days and washed with 70% alcohol solutions. Before mechanical tests, the samples were annealed on a hot plate at 70 °C for 24 h. For samples with selective mineralization, we used permeable fabrics to cover the polymer scaffolds and then immersed the sample into the BPU and mineralization medium. The fabric was used to prevent the mineralization on the sample surface and allow for the mineral growth within the selected regions.

*Characterization of Bionic Mineralized Composites*: The bionic composites were imaged with a Canon camera, a Nikon microscope, a scanning electron microscope (Nova NanoSEM 450), and a Micro-CT instrument (Zeiss/Xradia 410 Versa), respectively. The effective stiffness of the bionic composites was measured with compressive tests (strain rate 10$^{-5}$ s$^{-1}$) using an Instron mechanical tester. The stiffness mapping on the composite surface was characterized using indentation tests with the Instron mechanical tester (Figure S5, Supporting Information). The three-point bending and single-notched bending tests of the bionic composites were also carried out using the Instron mechanical tester. The flexural strength is calculated as $\sigma_f = 3SF_{max}/(2BW^2)$, where $F_{max}$ is the maximum load under the three-point bending, $S$ is the supporting span, $B$ is the sample width, and $W$ is the sample depth (Table S2, Supporting Information). The absorbed energy until failure is the enclosed area of the load–displacement curve of the three-point bending test. The crack-resistance curves determined by the sing-notched bending tests with an initial crack depth of 0.4 mm. The algorithm for the crack-resistance curve is described in Supporting Information.

*Phase-Field Simulation of Mineral Growth*: The formulation for the phase-field method is described in Supporting Information. The phase-field simulations were carried out using PDE module in COMSOL 5.4 Multiphysics. The simulation accuracy was verified by refining the mesh.

## Supporting Information

Supporting Information is available from the Wiley Online Library or from the author.

## Acknowledgements

## Conflict of Interest

The authors declare no conflict of interest.

## Data Availability Statement

The data that support the findings of this study are available from the corresponding author upon reasonable request.

[1] M. A. Meyers, P.-Y. Chen, A. Y.-M. Lin, Y. Seki, *Prog. Mater. Sci.* **2008**, *53*, 1.

[2] U. G. K. Wegst, H. Bai, E. Saiz, A. P. Tomsia, R. O. Ritchie, *Nat. Mater.* **2015**, *14*, 23.

[3] W. Huang, D. Restrepo, J. Y. Jung, F. Y. Su, Z. Liu, R. O. Ritchie, J. McKittrick, P. Zavattieri, D. Kisailus, *Adv. Mater.* **2019**, *31*, 1901561.

[4] H. D. Espinosa, A. L. Juster, F. J. Latourte, O. Y. Loh, D. Gregoire, P. D. Zavattieri, *Nat. Commun.* **2011**, *2*, 173.

[5] E. A. Zimmermann, B. Gludovatz, E. Schaible, N. K. N. Dave, W. Yang, M. A. Meyers, R. O. Ritchie, *Nat. Commun.* **2013**, *4*, 2634.

[6] J. C. Weaver, G. W. Milliron, A. Miserez, K. Evans-Lutterodt, S. Herrera, I. Gallana, W. J. Mershon, B. Swanson, P. Zavattieri, E. DiMasi, D. Kisailus, *Science* **2012**, *336*, 1275.

[7] Z. Tang, N. A. Kotov, S. Magonov, B. Ozturk, *Nat. Mater.* **2003**, *2*, 413.

[8] Z. Yin, F. Hannard, F. Barthelat, *Science* **2019**, *364*, 1260.

[9] L. J. Bonderer, A. R. Studart, L. J. Gauckler, *Science* **2008**, *319*, 1069.

[10] H.-L. Gao, S.-M. Chen, L.-B. Mao, Z.-Q. Song, H.-B. Yao, H. Cölfen, X.-S. Luo, F. Zhang, Z. Pan, Y.-F. Meng, Y. Ni, S.-H. Yu, *Nat. Commun.* **2017**, *8*, 287.

[11] S. Deville, E. Saiz, R. K. Nalla, A. P. Tomsia, *Science* **2006**, *311*, 515.

[12] E. Munch, M. E. Launey, D. H. Alsem, E. Saiz, A. P. Tomsia, R. O. Ritchie, *Science* **2008**, *322*, 1516.

[13] F. Bouville, E. Maire, S. Meille, B. Van de Moortèle, A. J. Stevenson, S. Deville, *Nat. Mater.* **2014**, *13*, 508.

[14] B. Yeom, T. Sain, N. Lacevic, D. Bukharina, S.-H. Cha, A. M. Waas, E. M. Arruda, N. A. Kotov, *Nature* **2017**, *543*, 95.

[15] L.i-B.o Mao, H.-L. Gao, H.-B. Yao, L. Liu, H. Cölfen, G. Liu, S.-M. Chen, S.-K. Li, Y.-X. Yan, Y.-Y. Liu, S.-H. Yu, *Science* **2016**, *354*, 107.

[16] R. M. Erb, R. Libanori, N. Rothfuchs, A. R. Studart, *Science* **2012**, *335*, 199.

[17] R. M. Erb, J. S. Sander, R. Grisch, A. R. Studart, *Nat. Commun.* **2013**, *4*, 1.

[18] H. L.e Ferrand, F. Bouville, T. P. Niebel, A. R. Studart, *Nat. Mater.* **2015**, *14*, 1172.

[19] F. L. Bargardi, H. L.e Ferrand, R. Libanori, A. R. Studart, *Nat. Commun.* **2016**, *7*, 1.

[20] J. J. Martin, B. E. Fiore, R. M. Erb, *Nat. Commun.* **2015**, *6*, 8641.

[21] Y. Yang, Z. Chen, X. Song, Z. Zhang, J. Zhang, K. K. Shung, Q. Zhou, Y. Chen, *Adv. Mater.* **2017**, *29*, 1605750.

[22] J. R. Raney, B. G. Compton, J. Mueller, T. J. Ober, K. Shea, J. A. Lewis, *Proc. Natl. Acad. Sci. USA* **2018**, *115*, 1198.

[23] Y. Yang, X. Li, M. Chu, H. Sun, J. Jin, K. Yu, Q. Wang, Q. Zhou, Y. Chen, *Sci. Adv.* **2019**, *5*, eaau9490.

[24] L. Addadi, D. Joester, F. Nudelman, S. Weiner, *Chem. Eur. J.* **2006**, *12*, 980.

[25] Y. Levi-Kalisman, G. Falini, L. Addadi, S. Weiner, *J. Struct. Biol.* **2001**, *135*, 8.

[26] H.-B. Yao, J. Ge, L.-B. Mao, Y.-X. Yan, S.-H. Yu, *Adv. Mater.* **2014**, *26*, 163.

[27] N. De Belie, E. Gruyaert, A. Al-Tabbaa, P. Antonaci, C. Baera, D. Bajare, A. Darquennes, R. Davies, L. Ferrara, T. Jefferson, *Adv. Mater. Interfaces* **2018**, *5*, 1800074.

[28] W. Li, B. Dong, Z. Yang, J. Xu, Q. Chen, H. Li, F. Xing, Z. Jiang, *Adv. Mater.* **2018**, *30*, 1705679.

[29] A. Xin, K. Yu, R. Zhang, B. Ruan, A. L. McGaughey, Z. Feng, K. H. Lee, Y. Chen, A. E. Childress, Q. Wang, *Mater. Horiz.* **2020**, *7*, 2130.

[30] S. S. Bang, J. K. Galinat, V. Ramakrishnan, *Enzyme Microb. Technol.* **2001**, *28*, 404.

[31] S. Stocks-Fisher, J. K. Galinat, S. S. Bang, *Soil Biol. Biochem.* **1999**, *31*, 1563.

[32] P. Anbu, C. H. Kang, Y. J. Shin, J. S. So, *SpringerPlus* **2016**, *5*, 250.

[33] T. Ghosh, S. Bhaduri, C. Montemagno, A. Kumar, *PLoS One* **2019**, *14*, e0210339.

[34] D. A. Porter, K. E. Easterling, *Phase Transformations in Metals and Alloys (revised reprint)*, CRC Press, Boca Raton, FL, USA **2009**.

[35] R. W. Balluffi, S. M. Allen, W. C. Carter, *Kinetics of Materials*, John Wiley & Sons, New York **2005**.

[36] M. She, Doctoral Dissertation, Massachusetts Institute of Technology, **2008**.

[37] N. Provatas, K. Elder, *Phase-Field Methods in Materials Science and Engineering*, John Wiley & Sons, New York **2011**.

[38] N. Suksangpanya, N. A. Yaraghi, D. Kisailus, P. Zavattieri, *J. Mech. Behav. Biomed. Mater.* **2017**, *76*, 38.

[39] N. Suksangpanya, N. A. Yaraghi, R. B. Pipes, D. Kisailus, P. Zavattieri, *Int. J. Solids Struct.* **2018**, *150*, 83.

[40] K. Wu, Z. Song, S. Zhang, Y. Ni, S. Cai, X. Gong, L. He, S.-H. Yu, *Proc. Natl. Acad. Sci. USA* **2020**, *117*, 15465.

[41] K. J. Koester, J. Ager, R. Ritchie, *Nat. Mater.* **2008**, *7*, 672.

[42] H. Peterlik, P. Roschger, K. Klaushofer, P. Fratzl, *Nat. Mater.* **2006**, *5*, 52.

[43] Q.-F. Guan, H.-B. Yang, Z.-M. Han, L.-C. Zhou, Y.-B. Zhu, Z.-C. Ling, H.-B. Jiang, P.-F. Wang, T. Ma, H.-A. Wu, *Sci. Adv.* **2020**, *6*, eaaz1114.

[44] M. Schaffner, P. A. Rühs, F. Coulter, S. Kilcher, A. R. Studart, *Sci. Adv.* **2017**, *3*, eaao6804.

[45] P. Q. Nguyen, N. D. Courchesne, A. Duraj-Thatte, P. Praveschotinunt, N. S. Joshi, *Adv. Mater.* **2018**, *30*, 1704847.

[46] M. S. Mannoor, Z. Jiang, T. James, Y. L. Kong, K. A. Malatesta, W. O. Soboyejo, N. Verma, D. H. Gracias, M. C. McAlpine, *Nano Lett.* **2013**, *13*, 2634.

[47] Y. L. Kong, M. K. Gupta, B. N. Johnson, M. C. McAlpine, *Nano Today* **2016**, *11*, 330.

# ADVANCED MATERIALS

## Supporting Information

Growing Living Composites with Ordered Microstructures and Exceptional Mechanical Properties

*An Xin, Yipin Su, Shengwei Feng, Minliang Yan, Kunhao Yu, Zhangzhengrong Feng, Kyung Hoon Lee, Lizhi Sun, and Qiming Wang\**

# Supporting Information

**Growing living composites with ordered microstructures and exceptional mechanical properties**

*An Xin[§], Yipin Su[§], Shengwei Feng, Minliang Yan, Kunhao Yu, Zhangzhengrong Feng, Kyung Hoon Lee, Lizhi Sun, and Qiming Wang\**

§Equal contribution
*E-mail: qimingw@usc.edu

## 1. Supplementary methods

## 1.1. Analytical model of mineral growth

In an oversaturated CaCO₃ solution with a molar concentration of $c_m$, solutes CaCO₃ aggregate to form minerals and grow starting from the lattice beam surface. The mineralization process is initiated by the bacterial nuclei.[1, 2] The molar concentration of CaCO₃ in the solid mineral is denoted as $c_p$. The molar concentration of CaCO₃ in the solution right around the solid mineral is $c_e$, which should be very low (e.g., 0.013 g/L).[3] Three concentrations should follow a relationship written as $c_p > c_m \gg c_e$. The solutes CaCO₃ in the solution around the mineral surface are absorbed to form the growing mineral. More CaCO₃ required to support the continuous mineral growth should be supplied by the diffusion of CaCO₃ solutes from the location away from the mineral surface. The concentration profile is shown in **Figure S1A**. The concentration of solute CaCO₃ in the solution should increase from $c_e$ at the location near the mineral surface to $c_m$ at the location far from the mineral surface.

The CaCO₃ molecules are supplied to the interface to form the solid mineral by diffusion. According to the Fick's first law,[4] the number of molecules CaCO₃ moving through the mineral interface within a time interval $dt$ can be calculated as

$$dN = D(2\pi r dz)\frac{\partial c}{\partial r}dt \qquad (S1)$$

where $D$ is the diffusion coefficient of CaCO₃ molecule within the solution, $r$ is the distance from the center of the lattice beam, $dz$ is the length along the beam length direction, and $c(r,t)$ is the instantaneous concentration of the solution at time $t$ and position $r$.

For the mineral interface to advance a distance $dr$ within a time interval $dt$, the incremental number of solute CaCO₃ within the mineral is

$$dN = (c_p - c_e)(2\pi r dz)dr \qquad (S2)$$

Equating Equation S1-S2 yields [1, 2, 5]

$$\frac{dr}{dt} = \frac{D}{c_p - c_e}\frac{\partial c}{\partial r} \qquad (S3)$$

To estimate $\partial c/\partial r$, we consider a simplified concentration profile shown in **Figure S1B**. We assume that the concentration of the CaCO₃ changes linearly from $c_e$ to $c_m$ along the distance of $L$ at the front of the mineral. The concentration gradient can be approximated as

$$\frac{\partial c}{\partial r} = \frac{c_m - c_e}{L} \qquad (S4)$$

The numbers of the solute CaCO₃ in the two shaded areas $A$ and $B$ in **Figure S1B** should be equal, i.e.,

$$\pi(r^2 - R^2)dz(c_p - c_m) = \pi[(r+L)^2 - r^2]dz\left(\frac{c_m - c_e}{2}\right) \qquad (S5)$$

We thus obtain $L$ as

$$L = \sqrt{r^2 \frac{2c_p - c_m - c_e}{c_m - c_e} - R^2 \frac{2c_p - 2c_m}{c_m - c_e}} - r \qquad (S6)$$

From Equation S3-S5, we have

$$\frac{dr}{dt} = \frac{D(c_m - c_e)}{(c_p - c_e)\left(\sqrt{r^2 \frac{2c_p - c_m - c_e}{c_m - c_e} - R^2 \frac{2c_p - 2c_m}{c_m - c_e}} - r\right)} \qquad (S7)$$

Since $C_e \ll C_m$ and $C_e \ll C_m$, Equation S7 can be reduced as

$$\frac{dr}{dt} = \frac{Dc_m}{c_p\left(\sqrt{r^2 \frac{2c_p - c_m}{c_m} - R^2 \frac{2c_p - 2c_m}{c_m}} - r\right)} \qquad (S8)$$

Considering that the mineral thickness is written as $H = r - R$, Equation S8 can be rewritten

as

$$\frac{d(H/R)}{d(Dt/R^2)} = \frac{1}{\frac{c_p}{c_m}\sqrt{(H/R + 1)^2\left(\frac{2c_p}{c_m} - 1\right) - \left(\frac{2c_p}{c_m} - 2\right)} - H/R - 1} \qquad (S9)$$

The initial condition is $H(t = 0) = 0$. We set $c_p/c_m = \alpha$, $H/R = Y$, and $Dt/R^2 = X$; then

we rewrite Equation S9 as

$$\left[\alpha\sqrt{(Y + 1)^2(2\alpha - 1) - (2\alpha - 2)} - Y - 1\right]dY = dX \qquad (S10)$$

Integrate Eq S10 from 0 to $X$, we obtain

$$\frac{\alpha(\alpha-1)}{\sqrt{2\alpha-1}}\left\{\left[(Y+1)\sqrt{\frac{2\alpha-1}{2\alpha-2}}\sqrt{\frac{2\alpha-1}{2\alpha-2}(Y+1)^2-1}-ln\left(\sqrt{\frac{2\alpha-1}{2\alpha-2}(Y+1)^2-1}+(Y+1)\sqrt{\frac{2\alpha-1}{2\alpha-2}}\right)\right]\right.$$

$$\left.-\left[\sqrt{\frac{2\alpha-1}{2\alpha-2}}-ln\left(\sqrt{\frac{1}{2\alpha-2}}+\sqrt{\frac{2\alpha-1}{2\alpha-2}}\right)\right]\right\}-\frac{Y^2}{2}-Y=X \qquad (S11)$$

In general, the normalized mineral thickness can be written as a function of time $t$ as

$$H/R = G(Dt/R^2, \alpha) \qquad (S12)$$

where $G()$ is a function of $Dt/R^2$ and $\alpha$. Using experimental parameter $R = 50\mu m$ and

estimated parameters $\alpha = 4.8$, $D = 5 \times 10^{-13} m^2/s$, we can obtain the relationship between

$H/R$ and mineralization growth time. Note that a certain period of $t_0$ is required to initiate the

mineral growth and the mineral growth starts at $t_0$. We can obtain the theoretically calculated

relationship between $H/R$ and $t$ (time of sample immersed in the mineralization medium),

plotted in **Figure 2E**.

**1.2. Phase-field modeling of mineral growth**

Mineral growth in the oversaturated CaCO3 medium can be simulated using a phase field

approach.[6] This model includes two variables: the phase field $\phi(x, t)$, and the concentration

field $c(x, t)$, both the fields are the functions of the position vector $x$ and time $t$. The variable

$\phi(x, t)$ is an ordering parameter, with $\phi = 0$ corresponding to liquid phase of CaCO3 and

$\phi = 1$ solid phase of CaCO3. The Helmholtz free energy of the system is [7]:

$$F(\phi, c) = \int_{\Omega}\left[f(\phi, c) + \frac{1}{2}\varepsilon^2(\nabla\phi)^2 + \frac{1}{2}k_c(\nabla c)^2\right]d\Omega \qquad (S13)$$

where $\Omega$ is the region occupied by the system, $f(\phi, c)$ is the Helmholtz free energy density

for a phase with no gradient. $\varepsilon$ is a small parameter which determines the thickness of the

interface of the two phases and $k_c$ is the interfacial coefficient. The specific normalized form

of $f(\phi, c)$ can be written as [7]:

$$f(\phi, c) = \frac{A_1}{2c_0^2}(c - c_1)^2 + \frac{A_2}{2c_0}(c_2 - c)\phi^2 + \frac{A_3}{3}\phi^3 + \frac{A_4}{4}\phi^4 \qquad (S14)$$

where $A_1 = 238.4, A_2 = 58, A_3 = -21.14, A_4 = 21.14$ are nondimensional constants, $c_1 = 0.288$ (mol/L) is a constant concentration, $c_2 = 0.6$ (mol/L) is the concentration of $CaCO_3$ within the solid mineral and $c_0 = 2.56$ (mol/L) is a constant concentration for nondimensionalization.

According to non-equilibrium thermodynamics,[6, 7] the evolution equations for the non-conserved phase-field variable $\phi$ and the conserved concentration-field variable $c$ can be written as the so-called Allen-Cahn [8] and Cahn-Hilliard [9] equations, respectively:

$$\tau \frac{\partial \phi}{\partial t} = -\frac{\delta F}{\delta \phi} \qquad (S15)$$

$$\frac{\partial c}{\partial t} = \nabla M \nabla \frac{\delta F}{\delta c} \qquad (S16)$$

where $M$ is related to atomic mobility of the solute and $\tau$ is related to the timescale for interfacial movement from the ordered phase to the disordered one.[6, 10] Both $M$ and $\tau$ are taken to be constants in this calculation.

Assuming $\varepsilon$ is a constant and using Equation S13, the differential equations S15 and S16 can be converted as following separately,

$$\tau \frac{\partial \phi}{\partial t} = \varepsilon^2 \nabla^2 \phi - \frac{\partial f}{\partial \phi} \qquad (S17)$$

$$\frac{\partial c}{\partial t} = M\left(-k_c \nabla^2 \nabla^2 c + \nabla^2 \frac{\partial f}{\partial c}\right) \qquad (S18)$$

For the specific energy density (Equation S14), the normalized governing equations describing time evolution of the inhomogeneous system can be obtained from Equation S17 and S18 as

$$\begin{cases} \bar{\tau}\dfrac{d\phi}{d\bar{t}} = \bar{\varepsilon}^2\bar{\nabla}^2\phi - A_4\phi^3 - A_3\phi^2 - A_2(\bar{c}_2 - \bar{c})\phi \\ \dfrac{d\bar{c}}{d\bar{t}} = \bar{M}\left(-\bar{k}_c\bar{\nabla}^2\bar{\nabla}^2\bar{c} + A_1\bar{\nabla}^2\bar{c} - \dfrac{A_2}{2}\bar{\nabla}^2\phi^2\right) \end{cases} \qquad (S19)$$

where the following dimensionless quantities have been introduced:

$$\bar{\tau} = \frac{D}{A_1 l^2}\tau, \bar{t} = \frac{D}{A_1 l^2}t, \bar{\varepsilon} = \frac{\varepsilon}{l}, \bar{c} = \frac{c}{c_0}, \bar{k}_c = \frac{k_c c_0^2}{l^2},$$

$$\bar{M} = \frac{MA_1}{c_0^2 D}, \bar{\nabla} = \left(\frac{\partial}{\partial\bar{x}} \quad \frac{\partial}{\partial\bar{y}}\right)^T = \nabla l, \bar{x} = \frac{x}{l}, \bar{y} = \frac{y}{l} \qquad (S20)$$

with $D$ being the diffusivity of the solute and $l$ the representative length of the system $\Omega$.

During the calculation, we use:

$$\bar{\tau} = 8.5 \times 10^{-5}, D = 5 \times 10^{-13}, l = 10^{-4}, \bar{M} = 1, \bar{k}_c = 2.98 \times 10^{-3}, \bar{\varepsilon} = 0.055 \qquad (S21)$$

We consider the boundary conditions:

$$\frac{\partial\phi}{\partial\boldsymbol{n}} = \frac{\partial c}{\partial\boldsymbol{n}} = 0 \qquad (S22)$$

where $\boldsymbol{n} = -\nabla\phi$ is the outward normal to the boundary $\partial\Omega$. Equation S22 means that there is no change in the total composition of the system due to transport across its boundary.

Initially, the concentration of the CaCO3 mineral and the solution are set as $c_2 = 0.6mol/L$ and, $c_m = 0.125mol/L$ respectively, so that oversaturation in the matrix provides the solute CaCO3 for crystallite growth. Finally, the evolution of the system can be solved from Equation S19 and S20 with the boundary condition S22 and the initial condition.

## 1.3. Calculation of fracture toughness

The fracture toughness for the crack initiation $K_{IC}$ is calculated using the following equation[11]

$$K_{IC} = \frac{F_{IC}S}{BW^{3/2}} \frac{3(\frac{a}{W})^{1/2}\left[1.99 - (\frac{a}{W})(1 - \frac{a}{W})(2.15 - \frac{3.93a}{W} + \frac{a^2}{W^2})\right]}{2(1 + \frac{2a}{W})(1 - \frac{a}{W})^{3/2}} \qquad (S23)$$

where $F_{IC}$ is the load in the single notched bending test corresponding to the crack initiation, $S$ is support span, $B$ is the width of the sample, $W$ is the depth of the sample, and $a$ is the notch depth (0.4 mm). The dimension parameters for samples in Figure 5 are shown in Table S1.

The fracture toughness during the crack propagation $K_{JC}$ is calculated from the elastic and plastic contribution,[12-16] written as

$$K_{JC} = \sqrt{JE'} \qquad (S24)$$

where $E' = E(1 - v^2)$, $E$ is Young's modulus, and $v$ is the Poisson's ratio. The J-integral is

$$J = J_{el} + J_{pl} \qquad (S25)$$

where $J_{el}$ is the elastic contribution and $J_{pl}$ is the plastic contribution. $J_{el}$ can be written as

$$J_{el} = K_{IC}^2/E' \qquad (S26)$$

$J_{pl}$ can be calculated as

$$J_{pl} = \frac{2A_{pl}}{B(W - a)} \qquad (S27)$$

where $A_{pl}$ is the plastic area underneath the load-displacement curve of the single notched bending test.

Crack extension $\Delta a$ can be calculated using the following algorithm,[12-16]

$$\Delta a = a_n - a \qquad (S28)$$

$$a_n = a_{n-1} + \frac{W - a_{n-1}}{2} \frac{u_n/f_n - u_{n-1}/f_{n-1}}{u_n/f_n} \qquad (S29)$$

where $u_n$ and $f_n$ are the displacement and force points on the single notched bending testing

curve after the crack initiation, respectively, and $a_n$ is the crack length.

## 2. Supplementary tables

**Table S1. Estimated information about the reported artificial structural composites shown in Fig. 1a.** The volume fraction data in Table S1 are the volume fractions of reported composites with the best mechanical performance. The reference numbers in Table S1 are different from those in the main text.

| Fabrication method | Reference number | Volume fraction of minerals | Possibility in forming mineral Bouligand structures |
|---|---|---|---|
| Layer-by-layer assembly | [17] | 99% | No |
| | [18] | 78% | No |
| Self-assembly | [19] | 50% | No |
| | [13] | 33.6% | No |
| Freeze-casting | [20] | 60% | No |
| | [21] | 80% | No |
| | [12] | 98.5% | No |
| Chemical Mineralization | [22] | 67% | No |
| | [14] | 86% | No |
| Field-induced mineral alignment integrated with casting | [23] | 14.2% | Possible but energy/time consuming |
| | [24] | 5-10% | Possible but energy/time consuming |
| | [25] | 60% (mineral-polymer composite) 90% (mineral-metal composites) 95.5% (mineral-ceramic composites) | Possible but energy/time consuming |
| | [26] | 10% | Possible but energy/time consuming |
| Field-induced mineral alignment integrated with 3D-printing | [27] | 15% | Yes |
| | [28] | 0.8% | Yes |
| | [29] | 18.5% | Yes |
| | [16] | 1.1% | Yes |

In reference [17], the volume fraction of mineral $CaCO_3$ was estimated by considering the occupied volume of the mineral in a characteristic volume of the sample: 1-3 nm*5.5x10$^{-15}$ m$^2$/(100 μm x 2.4 μm x 1 cm)≈99%. In reference [18], the volume fraction of glass within the glass-polymer laminate was estimated as 220 μm /(220 μm + 125 μm*50%)=78%. In reference [25], the volume fraction of mineral within mineral-polymer composites is 60%, within mineral-metal composites 90%, and within mineral-ceramic composites 95.5%. In reference [28], the composites with the best performance featured 1.5 wt% of MWCNT. Considering the density of the polymer resin as ~1200 kg/m$^3$ and the density of MWCNT as ~2250 kg/m$^3$, the volume fraction of MWCNT can be estimated as ~0.8%. In reference [16],

the composites with the best performance featured 2 wt% of graphene. The volume fraction of graphene can be estimated as 1.1%. In reference [12-14, 19-24, 26, 27, 29], the volume fractions of minerals were directly given in the papers.

**Table S2. Sample geometry information for four types of bionic mineralized composites in Figure 5.**

| Parameter | Type I | Type II | Type III | Type IV |
|---|---|---|---|---|
| Depth $W$ (mm) | 2.87 | 2.86 | 2.79 | 2.76 |
| Width $B$ (mm) | 5.61 | 5.39 | 5.33 | 5.45 |
| Length (mm) | 11.8 | 11.9 | 13.5 | 13.8 |
| Weight (g) | 0.222 | 0.223 | 0.236 | 0.230 |
| Support span $S$ (mm) | 11.4 | 11.4 | 11.4 | 11.4 |

**Table S3. Estimated specific flexural strength, specific fracture toughness, and absorbed energy density until failure of selected structural composites.** The reference numbers in Table S3 are different from those in the main text. The data were directly extracted from the respective papers.

| Structural composites | specific flexural strength $\sigma_f/\rho$ [$MPa/(Mg/m^3)$] | specific plateau fracture toughness $K_{JC}/\rho$ [$MPa \cdot m^{1/2}/(Mg/m^3)$] | absorbed energy density until failure $W_a$ [$MJ/m^3$] |
|---|---|---|---|
| Natural nacre[13, 14, 16] | 40-100 | 1.5-5 | 0.01-3 |
| calcium phosphate-alginate composites[13] | 120-140 | 3.5-4.4 | 0.01-4 |
| alumina-polymethyl methacrylate composites[21] | 65-90 | 1.5-5 | 0.01-4 |
| calcium carbonate-chitosan composites[14] | 30-60 | 0.6-1.3 | 17-20 |
| graphene-polymer composites[16] | 60-70 | 1.8-2.2 | 0.01-1 |
| Mineral-polymer composites (Type IV in Fig 5) | 76±8.7 | 2.63±0.3 | 20.26±2.35 |

**3. Supplementary figures**
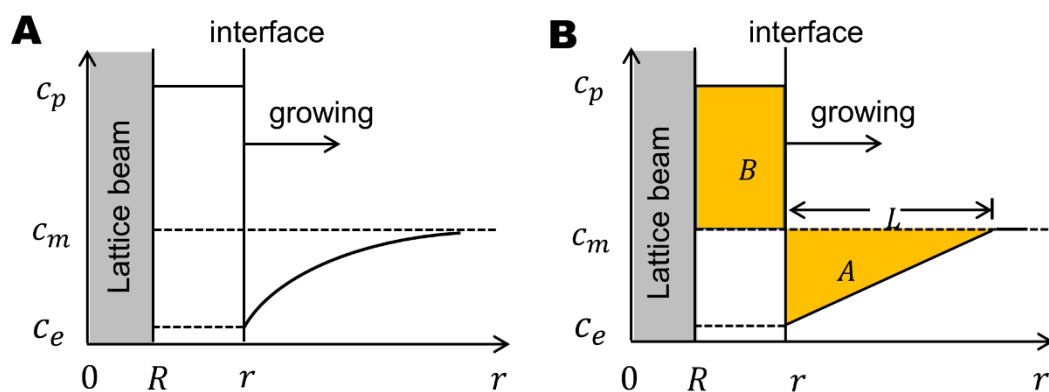


**Figure S1. Mineral growth model.** (A) Concentration profile of solute $CaCO_3$. (B) Simplification of the concentration profile.
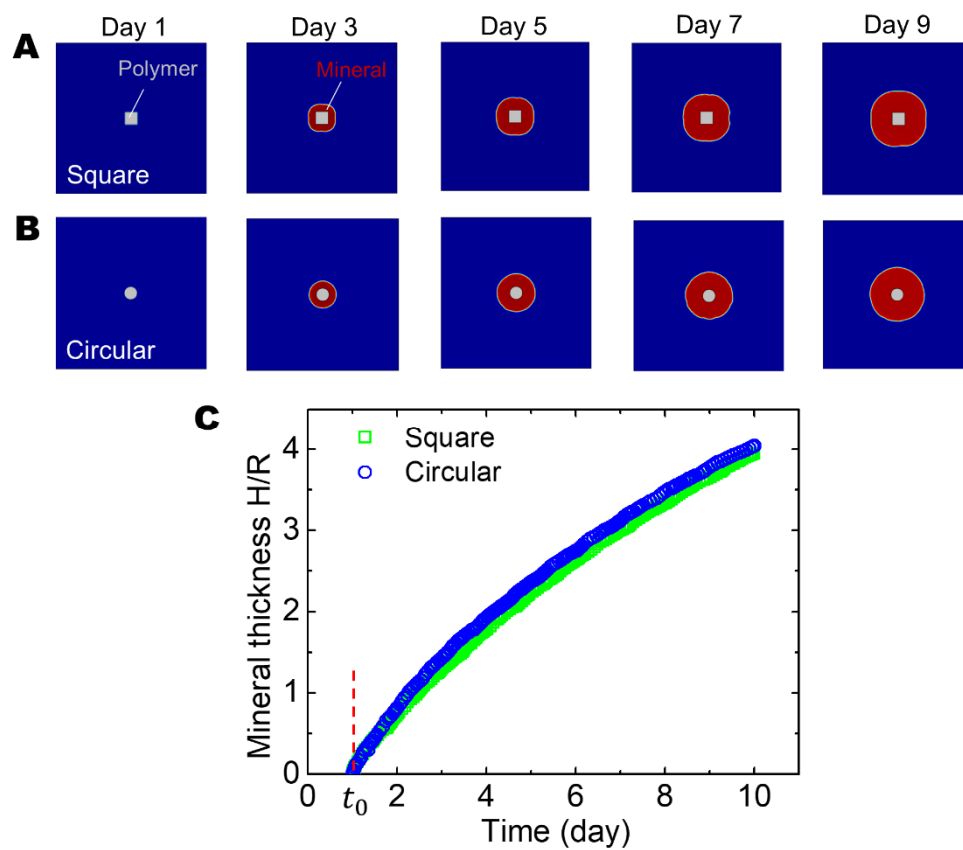
**Figure S2.** Phase-field simulation of mineral growth around (A) square and (B) circular beam cross-sections. (C) The normalized mineral thickness ($H/R$) around the polymers with square and circular cross-sections.
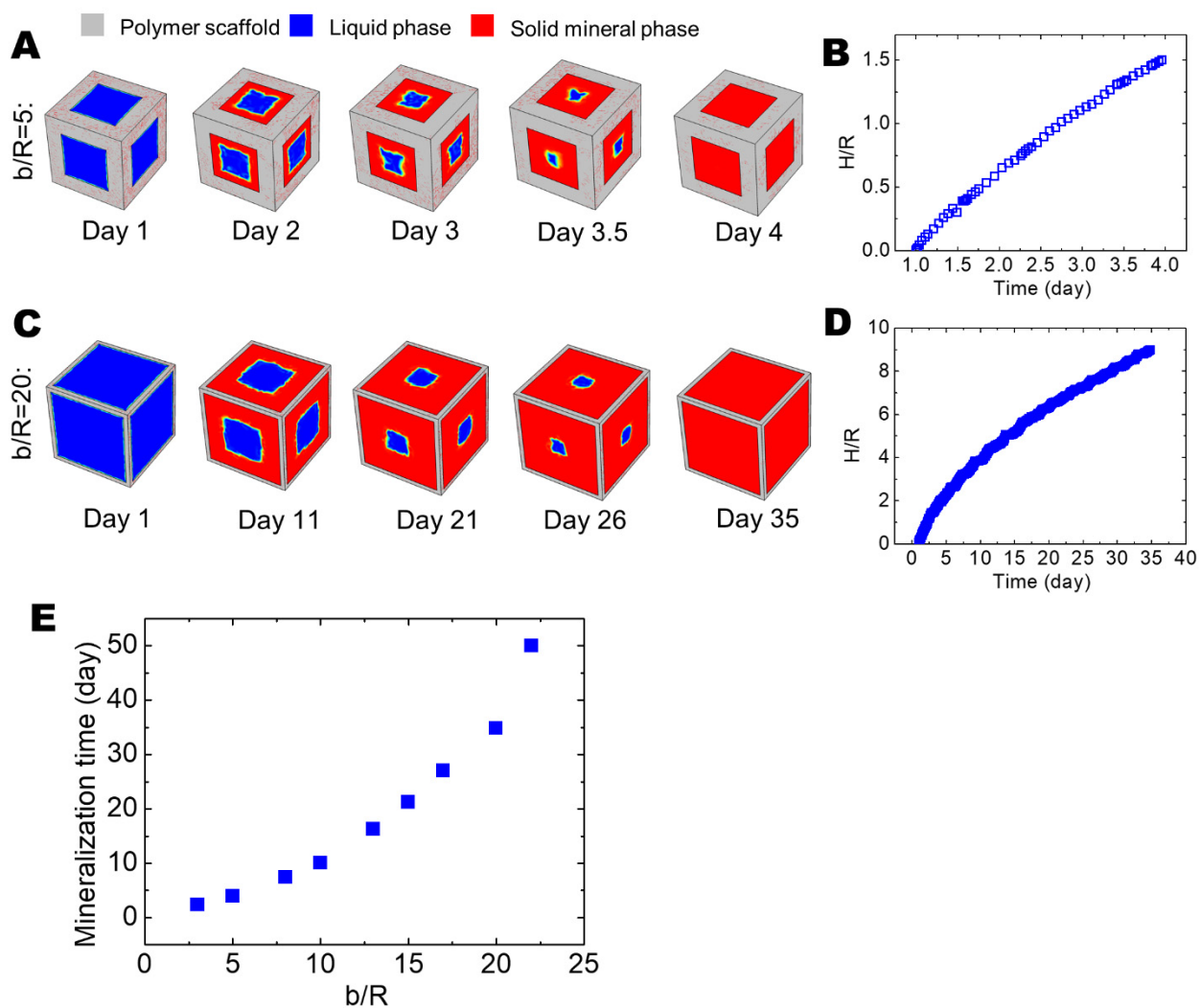
**Figure S3. Phase-field simulation of mineral growth within lattice units with different aspect ratios $b/R$.** (A) Phase-field simulation of mineral growth and (B) normalized mineral thickness $H/R$ for $b/R = 5$. (C) Phase-field simulation of mineral growth and (D) normalized mineral thickness $H/R$ for $b/R = 20$. (E) Required full mineralization time for lattice unit cells with various aspect ratios $b/R$.
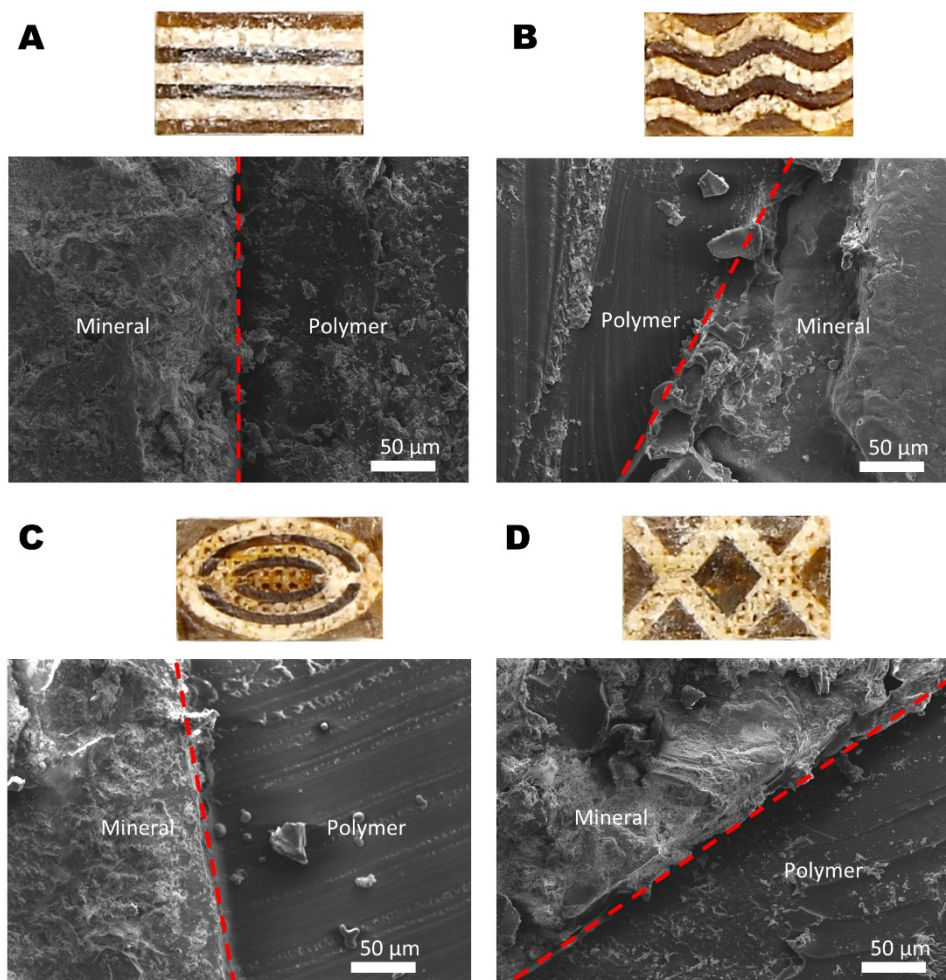
**Figure S4. SEM images to illustrate the cross-section interface between the mineral and polymer phases of four composites.**
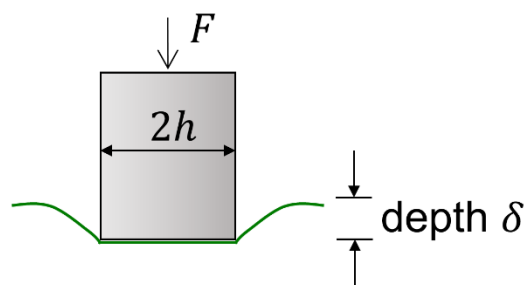
**Figure S5. Schematic for the indentation test**. A round-flat end cylinder indenter with radius R=0.3 mm is loaded to indent the sample by applying force F to a certain indentation depth $\delta$. The Young's modulus is calculated as $E = F(1 - v^2)/(2R\delta)$, where $v$ is the Poisson's ratio.
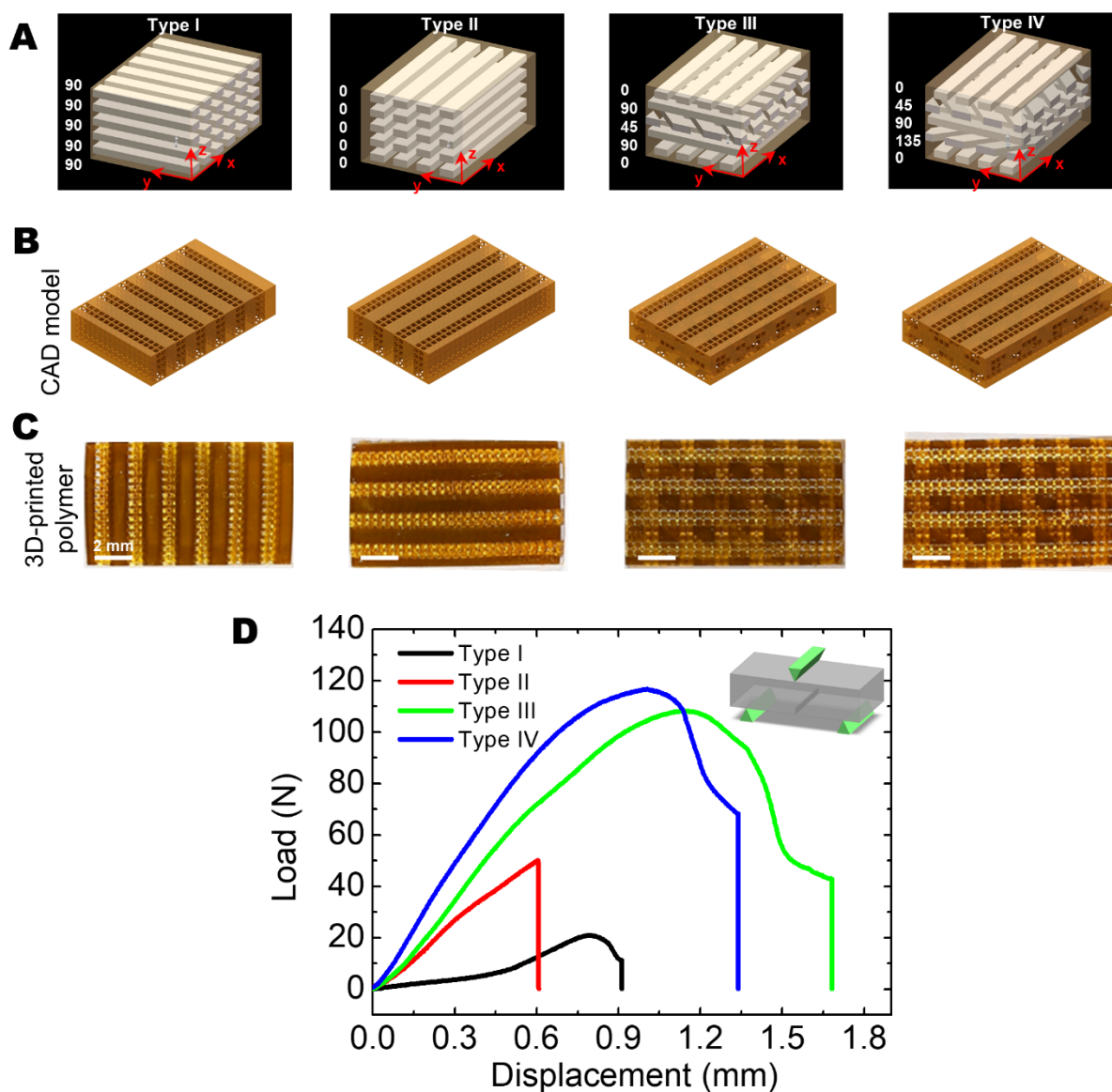
**Figure S6. Bionic mineralized composites with various mineral ply orientations**. (A) Schematics to illustrate ply orientations of mineral fibers on different layers of composites. The orientation angle is defined as the angle with x-axis. (B) Computer-aided design (CAD) models for polymer scaffolds. (C) 3D-printed polymer scaffolds. (D) Load-displacements for four types of composites under single-notched bending tests. The inset shows the schematic for the single-notched bending test.
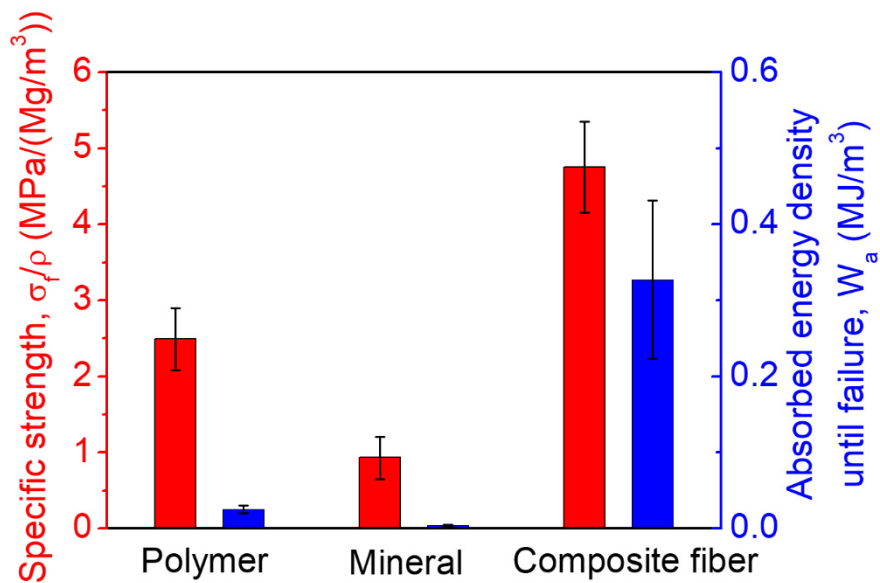
**Figure S7.** Specific flexural strengths and absorbed energy densities until failure of the pure polymer, the pure mineral, and the mineral-polymer composite fiber (minerals within polymer lattices). The error bars are standard deviations of 2-4 tests.

### 4. Captions of Supplementary movies

**Movie S1**: Amination to show the experimental procedure for growing bionic mineralized composites.

**Movie S2**: Phase-field simulation amination of mineral growth within a lattice with aspect ratio of *b/R*=10.

**Movie S3**: CT-scanned microstructure of type I composite.

**Movie S4**: CT-scanned microstructure of type II composite.

**Movie S5**: CT-scanned microstructure of type III composite.

**Movie S6**: CT-scanned microstructure of type IV composite.

# References

[1]     D. A. Porter, K. E. Easterling, M. Sherif, *Phase Transformations in Metals and Alloys, (Revised Reprint)*, CRC press, 2009.

[2]     R. W. Balluffi, S. Allen, W. C. Carter, *Kinetics of materials*, John Wiley & Sons, 2005.

[3]     F. W. Tegethoff, J. Rohleder, E. Kroker, *Calcium carbonate: from the Cretaceous period into the 21st century*, Springer Science & Business Media, 2001.

[4]     D. A. Porter, K. E. Easterling, *Phase transformations in metals and alloys (revised reprint)*, CRC Press, 2009.

[5]     C. Zener, Journal of applied physics 1949, 20, 950.

[6]     N. Provatas, K. Elder, 2011.

[7]     M. She, 2008.

[8]     J. W. Cahn, S. M. Allen, Le Journal de Physique Colloques 1977, 38, C7.

[9]     J. W. Cahn, J. E. Hilliard, The Journal of Chemical Physics 1958, 28, 258.

[10]    R. Kobayashi, Physica D 1993, 63, 410.

[11]    A. I. C. E. o. Fatigue, F. S. E. o. F. Mechanics, *Standard Test Method for Linear-elastic Plane-strain Fracture Toughness K [Ic] of Metallic Materials*, ASTM International, 2013.

[12]    F. Bouville, E. Maire, S. Meille, B. Van de Moortèle, A. J. Stevenson, S. Deville, Nature materials 2014, 13, 508.

[13]    H.-L. Gao, S.-M. Chen, L.-B. Mao, Z.-Q. Song, H.-B. Yao, H. Cölfen, X.-S. Luo, F. Zhang, Z. Pan, Y.-F. Meng, Y. Ni, S.-H. Yu, Nature Communications 2017, 8, 287.

[14]    Li-Bo Mao, H.-L. Gao, H.-B. Yao, L. Liu, H. Cölfen, G. Liu, S.-M. Chen, S.-K. Li, Y.-X. Yan, Y.-Y. Liu, S.-H. Yu, Science 2016, 354, 107.

[15]    H. Bai, F. Walsh, B. Gludovatz, B. Delattre, C. Huang, Y. Chen, A. P. Tomsia, R. O. Ritchie, Advanced Materials 2016, 28, 50.

[16]    Y. Yang, X. Li, M. Chu, H. Sun, J. Jin, K. Yu, Q. Wang, Q. Zhou, Y. Chen, Science Advances 2019, 5, eaau9490.

[17]    Z. Tang, N. A. Kotov, S. Magonov, B. Ozturk, Nature Materials 2003, 2, 413.

[18]    Z. Yin, F. Hannard, F. Barthelat, Science 2019, 364, 1260.

[19]    L. J. Bonderer, A. R. Studart, L. J. Gauckler, Science 2008, 319, 1069.

[20]    S. Deville, E. Saiz, R. K. Nalla, A. P. Tomsia, Science 2006, 311, 515.

[21]    E. Munch, M. E. Launey, D. H. Alsem, E. Saiz, A. P. Tomsia, R. O. Ritchie, Science 2008, 322, 1516.

[22]    B. Yeom, T. Sain, N. Lacevic, D. Bukharina, S.-H. Cha, A. M. Waas, E. M. Arruda, N. A. Kotov, Nature 2017, 543, 95.

[23]    R. M. Erb, R. Libanori, N. Rothfuchs, A. R. Studart, Science 2012, 335, 199.

[24]    R. M. Erb, J. S. Sander, R. Grisch, A. R. Studart, Nature communications 2013, 4, 1.

[25]    H. Le Ferrand, F. Bouville, T. P. Niebel, A. R. Studart, Nature Materials 2015, 14, 1172.

[26]    F. L. Bargardi, H. Le Ferrand, R. Libanori, A. R. Studart, Nature communications 2016, 7, 1.

[27]    J. J. Martin, B. E. Fiore, R. M. Erb, Nature Communications 2015, 6, 8641.

[28]    Y. Yang, Z. Chen, X. Song, Z. Zhang, J. Zhang, K. K. Shung, Q. Zhou, Y. Chen, Advanced materials 2017, 29, 1605750.

[29]    J. R. Raney, B. G. Compton, J. Mueller, T. J. Ober, K. Shea, J. A. Lewis, Proceedings of the National Academy of Sciences 2018, 115, 1198.